Biosensors and Bioelectronics 78 (2016) 14–22

Contents lists available at ScienceDirect

Biosensors and Bioelectronics

journal homepage: www.elsevier.com/locate/bios

A new nano-worm structure from gold-nanoparticle mediated random curving of zinc oxide nanorods

Veeradasan Perumal [a], Uda Hashim [a,b,*], Subash C.B. Gopinath [a], R. Haarindraprasad [a], P. Poopalan [b], Wei-Wen Liu [a], M. Ravichandran [c], S.R. Balakrishnan [a], A.R. Ruslinda [a]

[a] Biomedical Nano Diagnostics Research Group, Institute of Nano Electronic Engineering (INEE), Universiti Malaysia Perlis (UniMAP), Kangar, Perlis, Malaysia
[b] School of Microelectronic Engineering, University Malaysia Perlis (UniMAP), Kuala Perlis, Perlis, Malaysia
[c] Department of Biotechnology, Faculty of Applied Sciences, Asian Institute of Medicine, Science & Technology (AIMST), Semelling, Bedong, Kedah, Malaysia

ARTICLE INFO

Article history:
Received 26 August 2015
Received in revised form
16 October 2015
Accepted 28 October 2015
Available online 30 October 2015

Keywords:
Nano-worm
Nanorod
Zinc Oxide
Gold nanoparticle
DNA
Cholera

ABSTRACT

Creating novel nanostructures is a primary step for high-performance analytical sensing. Herein, a new worm like nanostructure with Zinc Oxide-gold (ZnO/Au) hybrid was fabricated through an aqueous hydrothermal method, by doping Au-nanoparticle (AuNP) on the growing ZnO lattice. During ZnO growth, fine tuning the solution temperature expedites random curving of ZnO nanorods and forms nano-worms. The nano-worms which were evidenced by morphological, physical and structural analyses, revealed elongated structures protruding from the surface (length: 1 μm; diameter: ~100 nm). The appropriate peaks for the face centred cubic gold were (111) and (200), as seen from X-ray diffractogram. The strong interrelation between Au and ZnO was manifested by X-ray photoelectron spectroscopy. The combined surface area increment from the nanoparticle radii and ZnO nanorod random curving gives raise an enhancement in detection sensitivity by increasing bio-loading. 'Au-decorated hybrid nano-worm' was immobilized with a probe DNA from Vibrio Cholera and duplexed with a target which was revealed by Fourier Transform Infrared Spectroscopy. Our novel Au-decorated hybrid nano-worm is suitable for high-performance bio-sensing, as evidenced by impedance spectroscopy, having higher-specificity and attained femtomolar (10 fM) sensitivity. Further, higher stability, reproducibility and re-generation on this sensing surface were demonstrated.

1. Introduction

Success in nanotechnology has been driven in most cases by bottom-up and top-down approaches with inter- and multi-disciplinary strategies (Gopinath et al., 2009; Fujimaki et al., 2010; Nomura et al., 2013; Simpson et al., 2011). These two approaches are highly involved in the creation of nanostructures, evidenced by a complete platform for research and development, forms roads from laboratory to Industry and bridging the gaps in all disciplines (Balakrishnan et al., 2015; Dong et al., 2010; Gopinath et al., 2008a; 2008b; Lakshmipriya et al., 2013). In laboratory conditions, bottom-up or self-assembly approaches, involving nanofabrication by chemical or physical forces operating at the nanoscale level to assemble basic units into complete structures, met great success (Li et al., 2011; McAlpine et al., 2007). In the recent years, with these approaches, nanostructured metal oxides have been the focus for biosensor development (Köck et al., 2014; Perumal and Hashim, 2013; Solanki et al., 2011). Among various types of nanostructured metal/semiconductor hybrids that have been developed, nanostructured Zinc oxide (ZnO) has been intensively studied because of its unique nano-morphology, functional biocompatibility, chemical stability, sensitivity, non-toxicity, and high catalytic properties (Foo et al., 2013; Jiang et al., 2014). Furthermore, ZnO nanostructures possess excellent electrical properties, which are suitable for fast and accurate sensing applications (Ali et al., 2012; Tak et al., 2014). The biocompatibility characteristics exhibited by ZnO is highly desired for surface functionalization and interfacing with chemical and biological compounds at pH extremes (Haarindraprasad et al., 2015; Liu et al., 2008; L. Wang et al., 2010a). Recently, optical, electrical and magnetic properties of ZnO nanostructure have been reported to be enhanced through the incorporation of novel metal nanoparticles, with advantages for improvements in biosensing characteristics owing to their potential for enhanced catalytic activity, surface to volume ratio and multiple functionality (Khoa et al., 2015; Kumar et al., 2015). It is expected that the judicious application of nanoscale structures via these combinations with novel metals, will yield new

* Corresponding author at: Biomedical Nano Diagnostics Research Group, Institute of Nano Electronic Engineering (INEE), Universiti Malaysia Perlis (UniMAP), Kangar, Perlis, Malaysia.
E-mail address: uda@unimap.edu.my (U. Hashim).

http://dx.doi.org/10.1016/j.bios.2015.10.083
0956-5663/

strategies and avenues for diagnosis and therapeutics (Geng et al., 2012; Lee et al., 2011). ZnO nanostructures prepared by bottom-up approach are catalytically synthesized by chemical and physical vapour depositions and vapour liquid solid method, where structures are assembled from basic units into larger structures (Suh et al., 2010; Wang et al., 2005). Unfortunately, bottom up approach through this method is not promising due to several limitations, such as low yield assembly, catalyst dependence, high cost and limited lab-settings, which require knowledge of complicated technologies (Bai et al., 2013; Kashif et al., 2013). Looking at ease of fabrication, sol–gel spin coating combined with an aqueous hydrothermal technique is an easy and convenient method for the synthesis of various ZnO nanostructures through the bottom-up approach. This technique has promising advantages, such as capability for production upscaling at low temperatures and production of epitaxial, anisotropic nanostructures (Polsongkram et al., 2008; Zhang and Que, 2010). Using this method and varying the growth parameters, such as reaction temperature, solution molarity, and pH, various ZnO nanostructure can be formed (Foo et al., 2014; Kashif et al., 2012; Perumal et al., 2015; Tak et al., 2014). However, there has not been much focus on the ZnO/Au hybrids to create novel nanostructures through the hydrothermal growth method. Herein, we report a new structure formation through AuNP mediated random curving of ZnO nanorod. In this study, we took the advantage of ZnO/Au properties and generated a new hybridized nanostructure possessing worm-like morphology on a silicon substrate. We demonstrated a simple, low-cost hydrothermal growth method to synthesize ZnO/Au hybrid worm, generated by doping Au on the ZnO nanorods. Further, the effects of AuNP on the surface topology, structural and optical characteristics of ZnO/Au hybrid nano-worm has been investigated. This study involves the process to obtain nano-worm like structure, the way developed remarkably creates an avenue for other new nanostructure creations.

2. Methods

2.1. Fabrication of Interdigitated Electrodes (IDEs)

A p-type silicon wafer was cleaned using RCA1, RCA2 and BOE to remove organic and inorganic contaminations and native oxide layer on the wafer surface (Adam and Hashim, 2014; Balakrishnan et al., 2014). Next, the silicon wafer was rinsed and cleaned with deionized water. 200 nm thick SiO_2 layer was produced on the cleaned wafer surface using a wet oxidation furnace. Using a conventional lithography process, an IDE device of 7 mm × 5 mm in size was patterned using negative resists (NR7-6000PY) on the SiO_2/Si substrate. A thermal evaporator (Auto 306 thermal evaporator; Edwards High Vacuum International, Wilmington, MA, USA) was used to deposit a Titanium/Au (500/3000Å) layer on the SiO_2/Si substrate and were patterned through lift-off process. Eventually, the negative photoresist sacrificial layer which formed was removed using acetone. In this work, an IDE with 16 fingers was fabricated where the width and length of each finger was 0.1 and 3.9 mm, respectively, and the spacing between the two adjacent fingers was 0.1 mm.

2.2. Preparation of ZnO thin films (ZnO-TFs)

ZnO-TFs were prepared using spin coating technique as follows; 8.78 g of $Zn(CH_3COO)_2 \cdot 2H_2O$ was dissolved in 200 ml of ethanol solvent (ZnO seed solution sol–gel). The concentration of ZnO was kept constant as 0.2 M. The mixed solution was then vigorously stirred with a magnetic stirrer at 60 °C for 30 min. The stabilizer, MEA was added drop by drop to the ZnO solution with constant stirring for 2 h. Finally, the transparent and homogenous solution were stored for aging at room temperature. The aged ZnO sol gel was deposited onto the IDE device by using a spin coating technique at a speed of 3000 rpm for 20 s. The deposition process of seed layer was repeated for 3 times to get a thicker ZnO thin film. For each deposition process, the coated ZnO thin films were dried at 150 °C for 20 min to remove the organic residuals that might exist on the ZnO thin films. The coated ZnO thin films were then annealed in a furnace under ambient air at 300 °C for 2 h to get highly crystallized ZnO.

2.3. Preparation of ZnO-TF–Au Nanohybrids

ZnO-TF–Au nanohybrids were prepared by a sputtering method. To form ZnO-TF–Au nanohybrids, Au wetting layer were physically deposited by a Sputter coater (EMS550X) with Au target and rotating stage. The detailed experimental condition is: electric current is kept at 25 mA, for 2–8 min and the Argon process vacuum level was kept at 10^{-2} mbar. Hence, we obtained Au- decorated ZnO TFs forming ZnO-TF–Au nano-hybrids.

2.4. Preparation of ZnO/Au hybrid nano-worm by hydrothermal method

ZnO Nano-worm like structure was formed using hydrothermal growth methods. For hydrothermal growth of ZnO/Au hybrid nano-worm, the prepared substrate with seed layer coated (ZnO-TF–Au nanohybrids) was submerged backward inside growth solution using Teflon sample holder. 25 mM of growth solution were prepared by mixing zinc nitrate hexahydrate and hexamethyltetramine in de-ionized water. The growth process was done inside a vacuum oven at 97 °C for 3 h. The prepared hydrothermal growth ZnO/Au hybrid nano-worm were cleaned with Isopropanol and de-ionized water to remove residual salt prior to annealing in furnace under ambient air at 300 °C for 2 h.

2.5. DNA immobilization and hybridization

The ZnO/Au hybrid nano-worm electrodes were cleaned and dried under nitrogen gas and used to fabricate DNA biosensor to detect *Vibrio cholera*. The direct immobilization of probe DNA on the electrode surface was achieved by dispensing 10 μL of 1 μM probe DNA solution in Tris- EDTA buffer for 3 h followed by washing the electrode and then rinsing with sterile double distilled water. The DNA hybridization was accomplished by dispensing the probe modified electrodes into different concentrations of test DNAs (complementary, non-complementary and mis-matches). The electrodes were washed upon hybridization process to remove any unbound target before measurements were taken. The complete immobilization process of thiolated probe DNA and hybridization with target is schematically illustrated in Fig. 2. The electrodes hybridized DNA was regenerated by rinsing the surfaces with hot (95 °C) deionized water for 2 min, followed by rapid cooling in ice bath. The surface was repetitively hybridized and regenerated with target for reusability test. The stability of probe DNA electrodes was studied for 4 weeks by performing the assay on a daily basis. Electrodes were stored in 4 °C when not in use.

3. Results and discussion

Utilizing a self-assembly bottom-up approach and nanoscale fabrication a new ZnO nanostructure possessing worm-like morphology was synthesized on silicon substrate. The doping of ZnO-TF with AuNPs (before the hydrothermal growth), created a new surface topography with the nano-worm structure. The heating

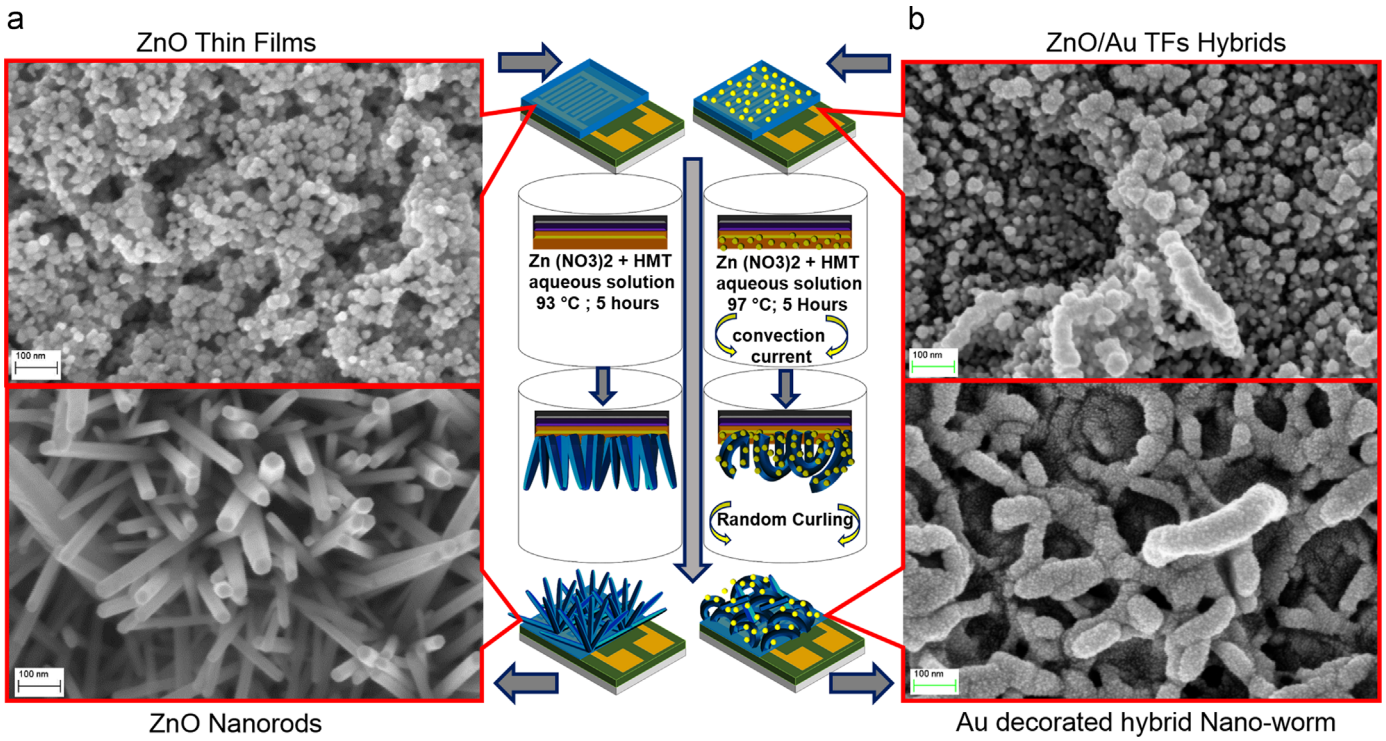

Fig. 1. Schematic illustration of differences in the steps involved for hydrothermal growth for Au-decorated hybrid nano-worm generation. For comparison ZnO nanorods (a), and Au-decorated hybrid nano-worm (b) are shown. Respective FESEM images are displayed.

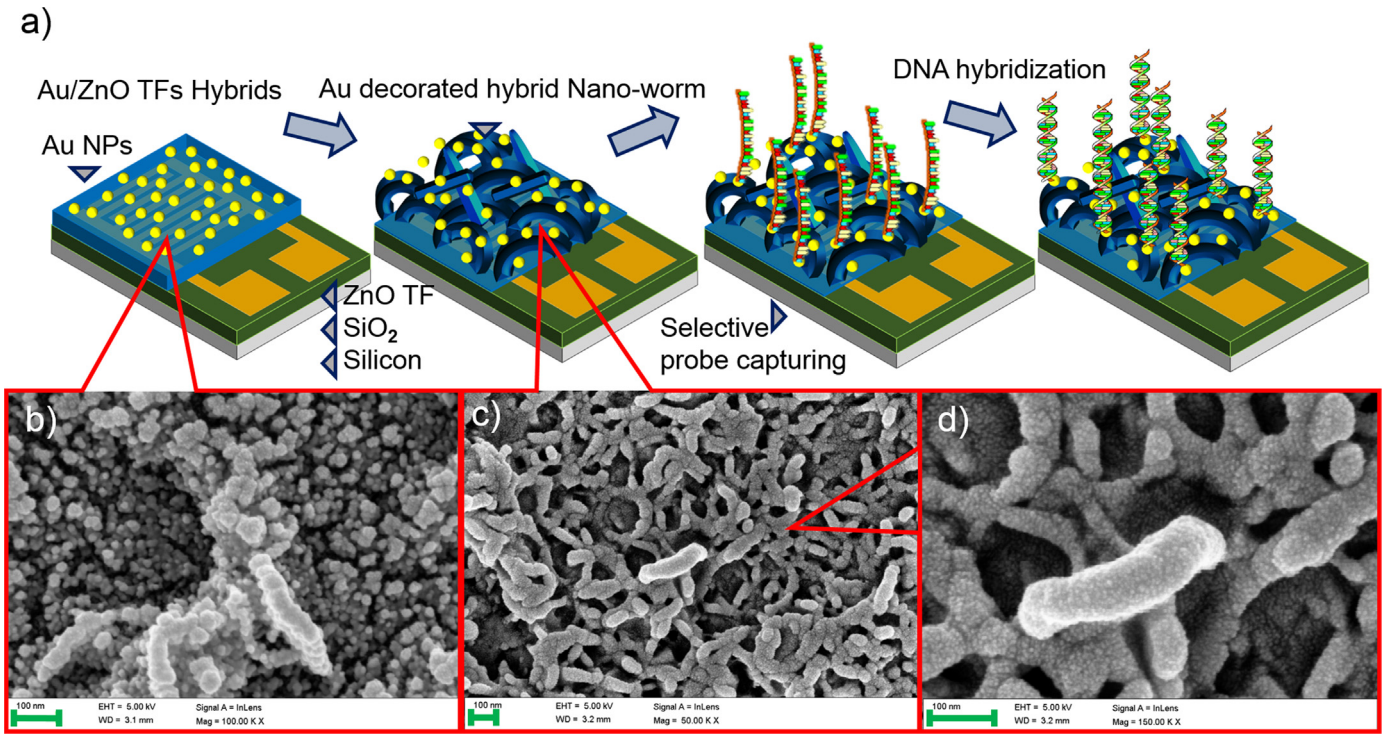

Fig. 2. (a) Schematic illustration represents the steps involved in the synthesis of "Au decorated hybrid nano-worm" DNA bioelectrode. (b) FESEM image of low magnification. Revealing surface of synthesized ZnO possess a worm like structure with Au nanoparticles agglomerates on the entire substrate surface. (c) Low and (d) high magnification image of "Au decorated hybrid nano-worm" indicate the worm like elongated structure protruding from the surface with average size of 1 μm length and diameter of ~100 nm.

process during hydrothermal growth produces a convection fluid-current in the growth solution which formed this nano-worm. The combined effects of convection current and heavy metal (Au) attachment causes the randomization of stress and strain at the surface of the substrate during nanorod formation, causing random curling and forming ZnO worm-like structure (herewith referred to as 'Au-decorated hybrid nano-worm'). Fig. 1(a,b) shows the schematic illustration of differences in the steps involved with hydrothermal growth for Au-decorated hybrid nano-worm in comparison to ZnO nanorods and displays the respective

morphological images. This Au-decorated hybrid nano-worm offers unprecedented nanostructures, having higher catalytic activity, sensitivity and stability to be employed in bio-sensing applications. A systematic study on the energetics of Au-decorated hybrid nano-worm systems is important for tailoring the properties of next-generation bio-nano devices. Hence, in this study we have characterized the intrinsic properties of Au-decorated hybrid nano-worm morphologically and structurally. Further, to elucidate the biosensing ability of Au-decorated hybrid nano-worm, we examined the biomolecular interactions using impedance spectroscopy.

3.1. Field-Emission Scanning Electron Microscopy (FESEM)

The general morphology of as-synthesized Au-decorated hybrid nano-worm was examined by FESEM. The results depicted from Fig. 2(a) showed the ZnO-TF–Au nanohybrids obtained after Au sputtering. The transformation of morphology from Au doped ZnO nano thin film to nano-particle assembled ZnO nano-worm after hydrothermal growth are depicted in Fig. 2(b) and (c), respectively. The FESEM image shown in Fig. 2(c), reveals the surface of the synthesized ZnO whereby Au agglomeration on the worm-like structure is seen for the entire substrate surface and with high density. A careful observation of the higher magnification FESEM (Fig. 2(d)) revealed that the worm-like elongated structure protruding from the surface with an average length of ~1μm and average diameter of ~100 nm. It can be seen that the worm-like morphology is surrounded by spherical nanoparticles of Au (bright spots). Clear agglomerations of the Au nanoparticles were observed on all surfaces of the worm-like ZnO matrices (Au-decorated hybrid nano-worm), demonstrating their homogeneity. The worm-like morphologies of ZnO matrix were substantially coarsened due to attachment of the AuNPs and contribute to a high surface area. This denotes an improvement over structural vacancy defects leading to the significant increase in surface area. Such improvement greatly facilitates the chemisorption of organic molecules, which is beneficial for the high loading of DNA during immobilization and hybridization process (Wang et al., 2012).

3.2. Transmission Electron Microscopy (TEM)

Structural morphology of the Au-decorated hybrid nano-worm composites were further examined under TEM. Fig. 3 depicts low and high magnifications of TEM analysis and selected area of electron diffraction pattern from the fabricated Au-decorated hybrid nano-worm. The low magnification TEM image on small parts of the specimens in Fig. 3a clearly shows the dark contrast, spherical structure of the AuNP exhibiting relatively good deposition on the surface of the nano-worm. The higher magnification TEM image, Fig. 3b reveals that the average diameter of nano-worm ~100 nm, which is in consistent with the observed FESEM results. The obtained image also shows the diameter of AuNPs deposited on the ZnO nano-worm is in the range of 5–40 nm and distributed homogenously on the surface of the ZnO nano-worm. As shown in Fig. 3c, the spherical structure of AuNP is observed as dark spots attached to the smooth ZnO nano-worm with diameter ~10 nm. Thus, AuNPs are seen to be stuck to the randomly curved ZnO structures – while agglomerating themselves, as seen in TEM images. This increases overall diameter of Au-decorated hybrid nano-worm structure over the plain ZnO nanorod. The observed inter-planar lattice fringe distance (0.24, 0.26 and 0.28 nm) of Au-decorated hybrid nano-worm corresponds to the spacing for Au (111) crystal planes and ZnO (100) and wurtzite ZnO (002) plane, respectively. This information suggested that both AuNPs and ZnO co-exist in a face centred cubic structure (Wu and Tseng, 2006; Ahmad et al., 2011). Supplementary Fig. S1(a–d) shows the corresponding SAED pattern of ZnO, AuNPs and ZnO/Au, respectively.

3.3. X-ray diffraction (XRD)

An X-ray diffraction analysis was carried out to examine the crystal quality, size, orientation and morphology of the fabricated Au-decorated hybrid nano-worm. As shown in Fig. 4a, the XRD spectra of both Au decorated hybrid nano-worm and pure ZnO are compared. The diffraction peaks corresponding to ZnO and Au matched the reported Joint Committee on Powder Diffraction Standards (JCPDS) reference spectra [for standard ZnO (No. 36–1451) and bulk Au (No. 65–2879)], which indicates the obtained spectra are in good agreement with standard JCPDS data cards. The obtained XRD patterns reflection peaks at 31.86° (100), 34.49° (002), 36.34° (101), 47.63° (102) and 56.65° (110) can be indexed as wurtzite phase of ZnO nanostructure (Fig. 4a–i). Interestingly, two additional diffraction peaks appear in Fig. 4a–ii, compared to pure wurtzite ZnO nanocrystals (Fig. 4a–i). The diffraction peak corresponding at 38.27° and 44.49° are assigned to diffraction lines of (111) and (200), respectively, which are indexed to face centred cubic of Au (Shan et al., 2008). Herein, (002) reflection appeared to be dominant for both samples which suggests that the hydrothermal ZnO nanostructure anisotropically prefers growth along the substrate (001) direction. The sharp and narrow diffraction peaks demonstrated that ZnO/Au nanocomposites have good crystalline quality. The crystallite structure of ZnO and AuNPs were

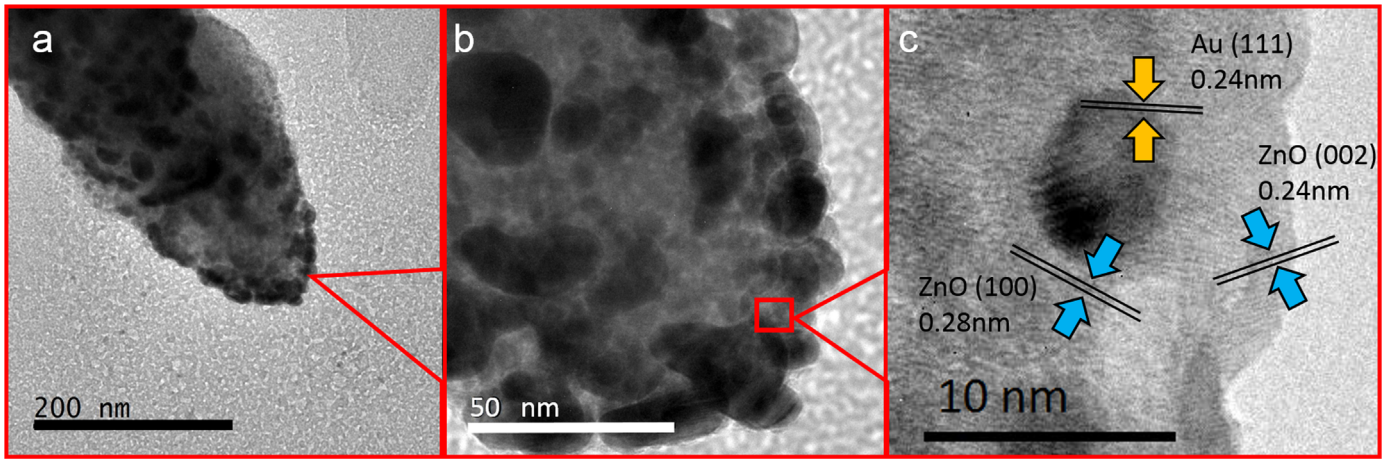

Fig. 3. (a) Typical TEM micrograph of Au decorated hybrid nano-worm. (b) High magnification TEM image. Revealed the average diameter of about 100 nm. (c) High Resolution TEM image. Showing the lattice fringes of Au and ZnO on Au decorated hybrid nano-worm.

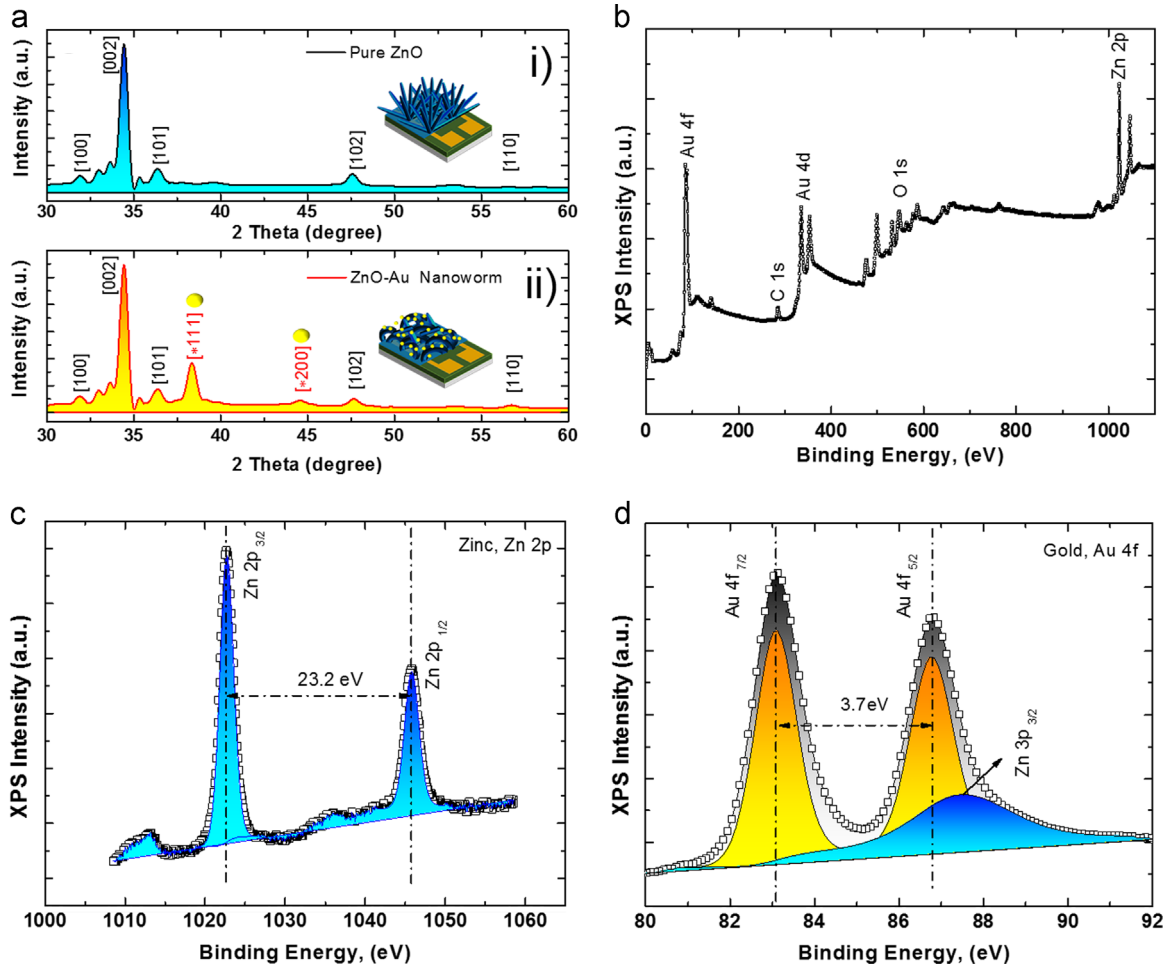

Fig. 4. (a) X-ray diffraction spectra. (i) Au-decorated hybrid nano-worm and (ii) bare ZnO. (b) Survey scan of XPS core level spectra taken on Au decorated hybrid nano-worm, showing binding energy of Zinc, Zn 2p (c) and gold, Au 4f electrons (d).

estimated using Scherrer equation. The crystallite sizes of Au-decorated hybrid nano-worm, estimated from the broadening of XRD peaks, are about 45.12 nm, whereas AuNP has 8.7 nm. The result is in good agreement with the HRTEM result. The lattice parameter indicated that the product was a composite material and no other impurities were present. Thus, the resultant planes demonstrated pure hexagonal wurtzite ZnO structure were synthesized with high-quality crystal and c-axis alignment.

3.4. X-ray photoelectron spectroscopy (XPS)

XPS studies were performed to reveal the elemental composition and chemical state of the elements present on the outmost layer of the hydrothermally grown Au- decorated hybrid nano-worm. The wide XPS survey scan has photoelectron peaks of carbon (C), oxygen (O), Zinc (Zn), and gold (Au) denoted from Au-decorated hybrid nano-worm without any impurities (Fig. 4b). The binding energies are calibrated within an accuracy of 0.1 eV using C1s (284.6). The corresponding gold Au 4f and zinc Zn 2p XPS spectra which were observed from Au-decorated hybrid nano-worm wide scan are enlarged in Fig. 4c and d, respectively. As shown in Fig. 4c, the Zn 2p XPS spectra consists of two peaks of Zn $2p_{3/2}$ and Zn $2p_{1/2}$ which correlate to binding energy peaks at 1022.63 and 1045.83, attributed to Zn^{2+} valance state (Wang et al., 2012). The observed Zn 2p binding energy of Au-decorated hybrid nano-worm has a slight positive shift compared with the corresponding value of pure ZnO. This further substantiated that Zinc and Au have interacted to form a compound with reduced structural vacancy defects in ZnO (Shan et al., 2008). Fig. 4d demonstrates the core level XPS spectra of Au 4f and Zn 3p. The binding energies of 83.14 eV, 86.84 eV and 87.8 eV corresponding to Au $4f_{7/2}$, $4f_{5/2}$ and Zn $3p_{3/2}$ were observed. The variation in Au $4f_{7/2}$ binding energy compared to 84.0 eV of bulk Au proved the strong electronic interaction between AuNPs and ZnO (Shan et al., 2008; Hosseini et al., 2015; Wang et al., 2015). The ZnO matrix has large structural defects caused by Zinc-and/or Oxygen-vacancies owing to its large surface to volume ratio and polycrystalline nature. The improvement in structural defect caused by zinc / oxygen vacancies is made possible by trapping Au atoms and facilitating the growth of Au-decorated hybrid nano-worms. Further discussion about the facts of the surface passivation effects on the Au-decorated hybrid nano-worm is discussed in Photoluminescence section which describes the shift in the corresponding binding energy of Au and Zn.

3.5. Photoluminescence (PL)

In order to correlate the optical properties of Au-decorated hybrid nano-worm with bare ZnO nanorods, PL analysis has been executed. Fig. 5a displays the PL characteristics exhibited by the ZnO nanorods and Au-decorated hybrid nano-worm. The bare ZnO nanorods show a weak near-band edge UV emission at 379 nm and a broad, strong green emission peak at 550 nm. In ZnO, the broad hump green emission corresponds to structural defects such as Zn- and/or O-vacancies. When the bare ZnO sample was excited at 325 nm, few electrons reached the conduction band while the

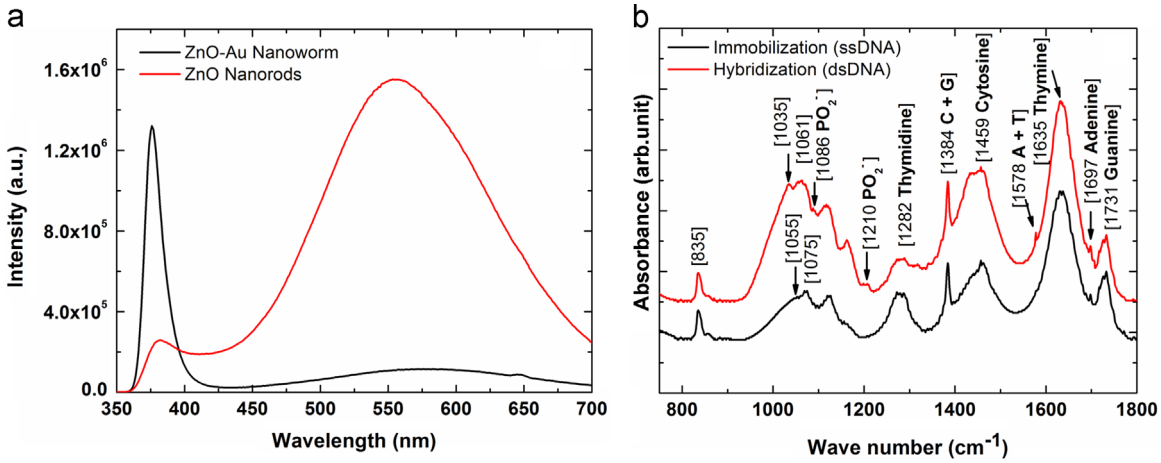

Fig. 5. (a) Photoluminescence spectra of Au decorated hybrid nano-worm compared with bare ZnO nanorods. (b) FTIR spectra Au-decorated hybrid nano-worm upon immobilization and hybridization of DNA sequences from *Vibrio Cholera*. Absorption regions are shown from 700 to 1800 cm^{-1}. (Au-decorated hybrid nano-worm/p-DNA (ssDNA) and Au-decorated hybrid nano-worm/p-DNA/t-DNA (dsDNA)).

majority of the electrons are still trapped in the defect levels. Thus, the electrons in the defect level readily recombined with the holes in the valence band of ZnO to give a broad hump over the visible emission. Moreover, the intensity of UV band emission was significantly reduced owing to lower recombination of electron–hole pairs from the conduction band (Geng et al., 2012; Kochuveedu et al., 2012). However, for the Au-decorated hybrid nano-worm sample the band edge emission intensity has been significantly increased by 6 folds. On the contrary, the defect related green emission has been highly suppressed almost to the noise floor. This complete suppression of green emission and increase in band edge emission is related to the novel metal (Au) introduction to the semiconducting ZnO structure. The energy level of ZnO defect states and Fermi level of Au are very close to each other. Therefore, the electrons from the defect level of ZnO can transfer to the surface plasmons of Au, which significantly increase the electron density of surface plasmons of Au. Consequently, when the surface plamons of Au are excited, prompting the electrons to elevate to higher energy states than the conduction band of ZnO (Cheng et al., 2010). These electrons could then be easily transferred back to the conduction band of ZnO, which facilitate the recombination of electron–hole pairs in the ZnO valance band (Dhara and Giri, 2011; Dhas et al., 2008). In short, the mechanism explains the enhancement in band edge emission and suppression of defect emission, which is achieved through AuNP mediated random curving of ZnO nanorod.

3.6. Immobilization and hybridization confirmation through Fourier Transform-Infrared (FTIR) spectroscopy

FTIR spectroscopy analysis was performed to investigate the structure of the compound and its vibrational characteristics present on the outmost layer of the Au-decorated hybrid nano-worm upon immobilization and hybridization of DNA sequences from Cholera. The FTIR spectra of Au-decorated hybrid nano-worm/p-DNA (probe) and Au-decorated hybrid nano-worm/p-DNA/t-DNA (duplexed) bio-electrode are shown in Fig. 5b. The transmission of infrared waves from FTIR is responsible for the identification of the various bonds in a functional groups of molecules via stretching and bending. In previous FTIR spectroscopic studies, the absorption region from 700 to 1800 cm^{-1} represents the fingerprint region of nucleic acid (Mello and Vidal, 2012). The comparison of the FTIR spectra of the immobilized (ss-DNA) and hybridized (ds-DNA) samples as indicated in Fig. 5b, reveals similar absorption peaks except for several differences. In ds-DNA, there is an apparent shift with the peak originally observed in ss-DNA at 900 cm^{-1} to the left-side of the spectrum (1250 cm^{-1}). The observation of ds-DNA spectra also revealed additional vibrational characteristics in the region of 900–1250. This is attributed to an increase in the amount of symmetric and asymmetric vibrations of PO_4^- group present in the DNA phosphodiester deoxyribose backbone resulting from the immobilization and hybridization process (Mello and Vidal, 2012; Petrovykh et al., 2003). The vibrational peak at 835 cm^{-1} revealed the presence of deoxyribose phosphate in both immobilized and hybridized samples. The FTIR spectra of Au-decorated hybrid nano-worm/p-DNA/t-DNA exhibits absorption peaks at 1035, 1061, 1086 and 1210 cm^{-1}, which correspond to the phosphate groups of DNA, such as the symmetric and anti-symmetric stretching of DNA phosphate, and phosphate back-boned stretching, respectively (Opdahl et al., 2007). This hints clearly about the success of immobilized and hybridized process on Au-decorated hybrid nano-worm lattice. Apart from this, the vibrational peaks at 1459, 1635, 1697 and 1731 cm^{-1}, corresponds to the functional groups of DNA, such as cytosine, thymine, adenine and guanine, respectively (Baker et al., 2008; Das et al., 2015). The corresponding absorption frequencies for the entire vibrational group observed in Fig. 5b with assignment and chemical moiety are shown in supplementary Table S1. These comprehensive FTIR results suggest that DNA molecules were successfully immobilized and hybridized onto the Au-decorated hybrid nano-worm.

3.7. Bio-sensing analyses on Au-decorated hybrid nano-worm

AC impedance spectroscopy has been used for bio-sensing analysis on Au-decorated hybrid nano-worm. Nyquist plots of the AC impedance spectroscopy spectra were obtained over the frequency range of 0–100 Mhz for a 100 mM PBS solution (pH 7.4) containing 10 mM $[Fe(CN)_6)]^{3-/4-}$ of the sample of bare Au-decorated hybrid nano-worm, Au-decorated hybrid nano-worm/p-DNA and Au-decorated hybrid nano-worm /p-DNA/t-DNA as shown in Fig. 6a. The obtained nyquist plot can be expressed by Randles equivalent circuit (inset), where the parameter Ra and Rct represent the resistance of bulk solution and charge transfer resistance respectively while CPE is an abbreviation for constant phase element. The semicircle in impedance spectra represents the interfacial charge transfer resistance, Rct, corresponding to the carrier transfer from the modified electrode to the ferricyanide in the solution. As shown in Fig. 6a, the semicircle (i) exhibits very small Rct value ($\sim$10.5 kΩ). The result suggests that interfacial

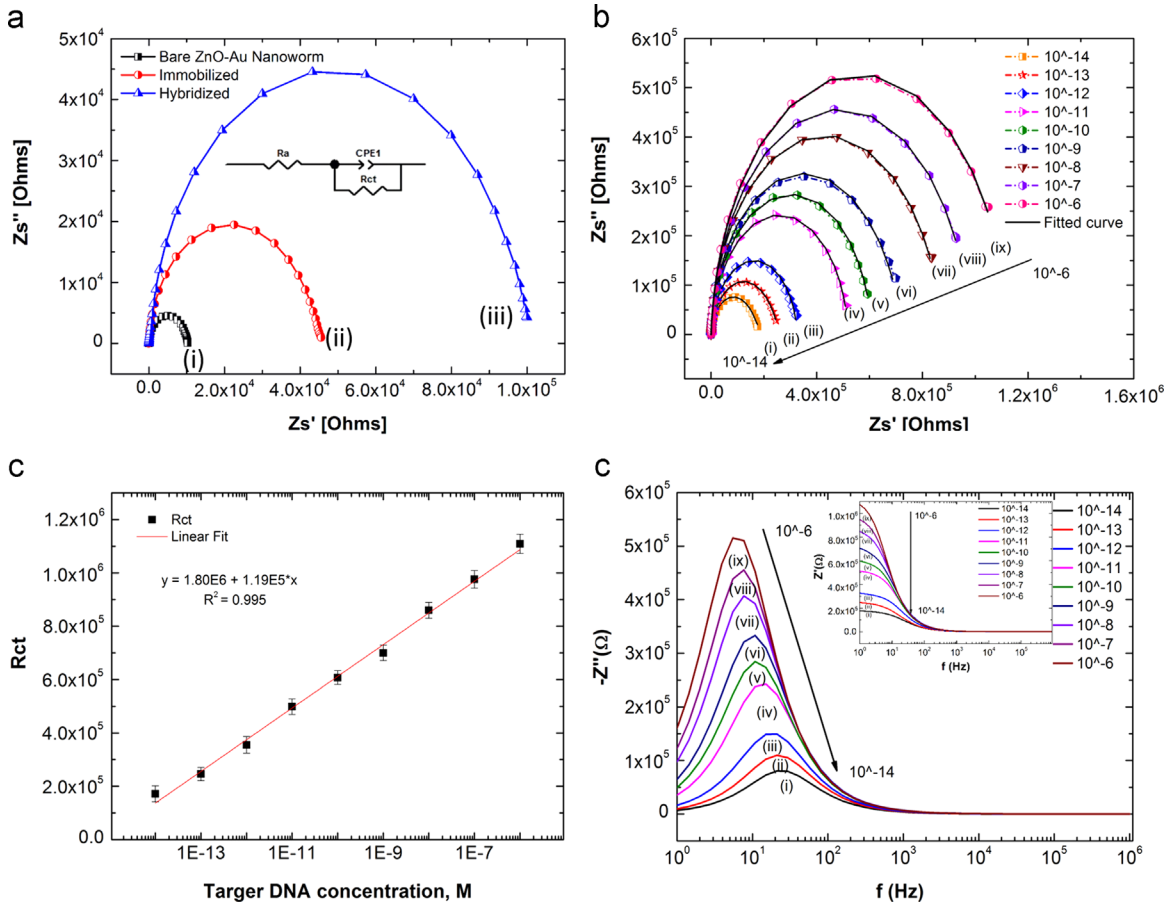

Fig. 6. (a) Impedance spectra of (i) Au decorated hybrid nano-worm, (ii) Au decorated hybrid nano-worm/p-DNA (probe) and (iii) Au decorated hybrid nano-worm/p-DNA/t-DNA (duplex) bio-electrode. The inset shows the Randles equivalent circuit, where the parameter Ra, Rct and CPE are representing the bulk solution resistance, charge transfer resistance and constant phase element, respectively (b) Impedimetric response curve of Au decorated hybrid nano-worm /p-DNA hybridized with different concentrations of complementary target DNA (i–ix) 0.1 mM to 1 pM. (c) Shows the linear regression curve for different concentrations of target DNA with linear equation of ΔRct, (d) Imaginary part showing overall impedance which decreases and the peak frequency shifted towards the higher frequencies as the concentration of complementary DNA decreases. Inset graph showing the gain curve of Au-decorated hybrid nano-worm /p-DNA hybridized with different concentrations.

layer of bare Au-decorated hybrid nano-worm has an excellent electron transfer property towards to electrolyte solution owing to its high surface area. There is an increment in the Rct (~45.5 kΩ) value observed upon immobilization of thiolated ssDNA probe with respect to the bare Au-decorated hybrid nano-worm. The observed diameter increment can be explained as the adsorption of the probe DNA following immobilization leading to Au–SH bond on the surface of the sample blocking the diffusion of $[Fe(CN)_6]^{3-/4-}$ towards the electrode surface leading to an increase of Rct (Häkkinen, 2012; Ramulu et al., 2013). Such increment in Rct value not only confirms the effective immobilization of the probe DNA but also reveals the electrostatic repulsion caused by the electro-negative phosphate skeleton of the DNA. Further increment in the Rct value (100.0 kΩ) for Au-decorated hybrid nano-worm/p-DNA/t-DNA was observed (Fig. 6a). It likely is caused by increasing the electro-negative phosphate skeleton of the DNA resultant of the hybridization process, which is attributed to the electrostatic repulsion force between the negatively charge phosphate backbone and $[Fe(CN)_6]^{3-/4-}$ anion at electrode surface. Thus, the resultant Rct value confirms the successful hybridization of target DNA towards the probe immobilized bio-electrode (Ohno et al., 2012; Ramulu et al., 2013). Nyquist plot of concentration dependent (10^{-6}–10^{-14}) DNA duplex formation between probe and the target DNA is shown in Fig. 6b. As seen in the figure, the Rct value increased upon hybridization with increasing concentration of target DNA. Thus, the observed increase in Rct value could be ascribed by the electrostatic repulsion between the $[Fe(CN)_6]^{3-/4-}$ anion and the negatively charged phosphate backbone of the complementary DNA. Supplementary Table S2 displays the simulation results with nonlinear curve fitting for the measured impedance with an equivalent circuit. The sensitivity of the proposed Au-decorated hybrid nano-worm bio-electrode was investigated and a linear correlation of differences in the charge transfer resistance, with respect to the logarithm of complementary DNA concentration is shown in Fig. 6c. It was observed that Rct linearly increases with increasing complementary DNA concentrations from 10 fM to 1 μM. The different values of Rct at probe for immobilized bio-electrode and hybridized bio-electrode were found to be proportional to the natural logarithm of t-DNA concentration with a linear equation of Rct = 1.5434E9x + 1.16923E8, (R^2 = 0.99026). Fig. 6d shows the imaginary part of impedance by plotting the imaginary (–Z") against the logarithm of the frequencies which exhibits Debye-type peaks. It is obvious that the imaginary part of overall impedance decreases and the peak frequency shifted towards the higher frequencies as the concentration of complementary DNA decreases. The decrease in imaginary part impedance indicates that conductivity of the sensor increases, whereas the shifting indicates that as the DNA concentration decreases, the relaxation time is increasing. Thus, decreasing the DNA concentration results in overall decrease in imaginary part impedance, which reflects the ease flow of the charge carriers to the AC electric field (Kashif et al., 2013; A. A. Saif and Poopalan, 2011a). The variation of the real (Z') components of impedance for various complementary DNA concentration with frequency reveals

a relaxation peak for Au-decorated hybrid nano-worm bio-electrode as shown in the inset of Fig. 6d. It can be observed from the results that the susceptibility of the sensor can be categorized to 3; the constant frequency range of 1–10 Hz, sharp decrement at 10–1000 Hz and a constant gain at 1000 Hz onwards. In principle, the enhanced space charge region rules the conductivity process during low frequency range. Further increase in the frequency results in sharp decrement in the susceptibility which is influenced by surface charge on the grains. At high frequencies ($\geq$ 1000 Hz) all curves are seen to be merging, which suggests that the measured impedance equals the static impedance at this stage (Saif and Poopalan, 2011b, 2011c). This comprehensive results leads to a suitable selection of frequency for optimization of the fabricated bio-electrode. The high-performance sensing of Au-decorated hybrid nano-worm can be derived from the following aspects; the oxygen molecules from ambient atmosphere can be easily adsorbed on ZnO owing to their large surface to volume ratio of ZnO nanostructures. This leads to a migration of electron from the conduction band of ZnO material towards oxygen, creating many electron traps at the grain boundary surfaces, which leads to broadening of depletion layer with lower conductivity (O_2 (gas)$+e^- = O_2^-$ (ads)) (Gogurla et al., 2014; Kashif et al., 2013). In the present study, ordinary physical structure of ZnO has been altered, where Au-decorated hybrid nano-worm structure was fabricated through hydrothermal growth process. However, the physical structure alteration does not change the ZnO tendency for n-type conductivity. The consequence of this fact is that the work function of ZnO is higher (5.2–5.3 eV) than Au (5.1 eV), resulting in an electron transfer from Au to ZnO (Ohmic junction) until the two systems reach a dynamic equilibrium at initial state (Janotti and Van de Walle, 2009; Zhang et al., 2012). This leads to a decrease in the width of the depletion layer with higher conductivity. On the other hand, in this manuscript we reported immobilization of thiolated DNA using a strong covalent bond between Au and sulphur. Hence, the immobilization of thiolated probe DNA on the AuNPs in the ZnO nano-composites alters the dynamic equilibrium of Au-decorated nano-worm. The covalent bond between Au and Sulphur gives rise to a hole current density on the ZnO surface induced by the negatively charged phosphate backbone, resulting in a decrease in the electron again leading to broadening of depletion layer which lowers the conductivity. Hence, this variation has been employed to elucidate the sensing mechanism at interfacial surface of bio-electrode during the immobilization and hybridization process, which leads to an alteration in its impedance.

3.8. Analytical performances of Au-decorated hybrid nano-worm biosensor

Further tests were conducted to evaluate the analytical performance of Au-decorated hybrid nano-worm bio-electrode, which are shown in Supplementary Fig. S2(a–d). In brief, Au-decorated hybrid nano-worm bio-electrode has good linearity and a detection limit to the level of femtomolar, which was estimated using a signal to noise ratio of more than 3σ. The Rct value of the t-DNA (1 nM) was ~498 kΩ, which is nearly 14 folds larger than single base mismatched DNA (~36.9 kΩ) with the same concentration, indicates DNA biosensor has excellent sequence specificity. Therefore, the sensitivity and specificity reported is among the best, compared to the previous reports in literatures (Das et al., 2010; Huang et al., 2015; Iyer et al., 2014; Ryu et al., 2010; J. Wang et al., 2010b; Zhang et al., 2008a, 2008b). The cross specificities with other bacteria, such as *Leptospira* and *E.coli* are also shown in Supplementary Fig. S2b. The value of Rct signal does not vary significantly in the presence of unrelated molecules, indicating non-influence of the individual interferants. The re-usability of the biosensor was tested by repetitive hybridization with t-DNA, the Rct values of the regenerated bio-electrode before and after hybridization were tested (Supplementary Fig. S2b; inset). After consequent 5 regenerations and hybridizations, the electrode only lost about 9.4% of its original Rct signal value. Therefore, the regeneration of the proposed DNA Au-decorated hybrid nano-worm sensor possessed potential for continuous analysis of target DNA. The electro-analytical response of Au-decorated hybrid nano-worm biosensor shown in Supplementary Fig. S2c, revealed that the response time for this DNA sensor can be 1 min with the complete duplex formation. The stability of shelf-life study results (Supplementary Fig. S2d) showed that the prepared bio-electrode is very stable and lost 50% of its activity only after 12 weeks. As shown in the inset (Supplementary Fig. S2d; inset), the reproducibility of developed Au-decorated hybrid nano-worm sensor has a relative standard deviation (R.S.D) of 3% with 5 parallel measurements prepared under similar processing conditions, which shows a good reproducibility of the fabricated DNA biosensor. Further, the comparison of analytical performance with different DNA sensor shown in Supplementary Table S3.

4. Conclusion

Fine tuning of the fabrication of metal hybrids created novel structures, and participation of Au or Au-colloids are predominant in these processes. The current study detailed the fabrication ZnO and AuNP colloid hybrid under a finely tuned hydrothermal method and succeeded with a new novel 'Au-decorated hybrid nano-worm'. This new nanostructure is shown to be created by a sequential random curving of ZnO upon doping with AuNP. Progression and completion of this structure was clearly demonstrated by different morphological, physical and electrical based analyses. Further, the ability of created Au-decorated hybrid nano-worm structure for impedance sensing was proved to distinguish *Vibrio Cholera*. A clear demonstration was displayed and attained the sensitivity to the level of femtomolar. Further, higher stability, reproducibility and regeneration on this sensing surface were demonstrated. The created nanostructure hybrid has thrown a bunch of ideas towards future novel nanostructure developments, a new direction towards nanotheranostics.

Acknowledgments

The authors would like to thank Ministry of Higher Education Malaysia for the financial support through MTUN-COE grant 9016-00004. We also would like to convey our sincere thanks to Universiti Malaysia Perlis (UniMAP) for giving the opportunities to conduct the research in the Nano Biochip Lab, Failure analysis lab and Microfabrication cleanroom. The appreciation also goes to all the team members and staffs in the Department of Biotechnology, Asian Institute of Medicine, Science and Technology University (AIMST), Institute of Nanoelectronic Engineering (INEE), and School of Microelectronic Engineering (SoME), UniMAP.

Appendix A. Supplementary material

Supplementary data associated with this article can be found in the online version at http://dx.doi.org/10.1016/j.bios.2015.10.083.

References

Adam, T., Hashim, U., 2014. Biosens. Bioelectron. 67, 656–661.
Ahmad, M., Yingying, S., Nisar, A., Sun, H., Shen, W., Wei, M., Zhu, J., 2011. J. Mater. Chem. 21, 7723.

Ali, S.M.U., Ibupoto, Z.H., Kashif, M., Hashim, U., Willander, M., 2012. Sensors 12, 2787–2797.
Bai, S., Sun, C., Guo, T., Luo, R., Lin, Y., Chen, A., Sun, L., Zhang, J., 2013. Electrochim. Acta 90, 530–534.
Baker, M.J., Gazi, E., Brown, M.D., Shanks, J.H., Gardner, P., Clarke, N.W., 2008. Br. J. Cancer 99, 1859–1866.
Balakrishnan, S.R., Hashim, U., Gopinath, S.C.B., Poopalan, P., Ramayya, H.R., Iqbal Omar, M., Haarindraprasad, R., Veeradasan, P., 2015. PLOS One 10, e0137891.
Balakrishnan, S.R., Hashim, U., Letchumanan, G.R., Kashif, M., Ruslinda, a R., Liu, W. W., Veeradasan, P., Haarindra Prasad, R., Foo, K.L., Poopalan, P., 2014. Sens. Actuators A Phys. 220, 101–111.
Cheng, C.W., Sie, E.J., Liu, B., Huan, C.H. a, Sum, T.C., Sun, H.D., Fan, H.J., 2010. Appl. Phys. Lett. 96, 3–5.
Das, M., Sumana, G., Nagarajan, R., Malhotra, B.D., 2010. Thin Solid Films 519, 1196–1201.
Das, T., Kutty, S.K., Tavallaie, R., Ibugo, A.I., Panchompoo, J., Sehar, S., Aldous, L., Yeung, A.W.S., Thomas, S.R., Kumar, N., Gooding, J.J., Manefield, M., 2015. Sci. Rep. 5, 8398.
Dhara, S., Giri, P.K., 2011. J. Appl. Phys., 110.
Dhas, V., Muduli, S., Lee, W., Han, S.-H., Ogale, S., 2008. Appl. Phys. Lett. 93, 243108.
Dong, A., Chen, J., Vora, P.M., Kikkawa, J.M., Murray, C.B., 2010. Nature 466, 474–477.
Foo, K.L., Hashim, U., Muhammad, K., Voon, C.H., 2014. Nanoscale Res. Lett. 9, 1–10.
Foo, K.L., Kashif, M., Hashim, U., 2013. Appl. Mech. Mater. 284–287, 347–351.
Fujimaki, M., Nomura, K., Sato, K., Kato, T., Gopinath, S.C.B., Wang, X., Awazu, K., Ohki, Y., 2010. Opt. Exp. 18, 15732–15740.
Geng, J., Song, G.H., Jia, X.D., Cheng, F.F., Zhu, J.J., 2012. J. Phys. Chem. C 116, 4517–4525.
Gogurla, N., Sinha, A.K., Santra, S., Manna, S., Ray, S.K., 2014. Sci. Rep. 4, 6483.
Gopinath, S.C.B., Awazu, K., Fons, P., Tominaga, J., Kumar, P.K.R., 2009. Anal. Chem. 81, 4963–4970.
Gopinath, S.C.B., Awazu, K., Fujimaki, M., Sugimoto, K., Ohki, Y., Komatsubara, T., Tominaga, J., Gupta, K.C., Kumar, P.K.R., 2008a. Anal. Chem. 80, 6602–6609.
Gopinath, S.C.B., Awazu, K., Tominaga, J., Kumar, P.K.R., 2008b. ACS Nano 2, 1885–1895.
Haarindraprasad, R., Hashim, U., Gopinath, S.C.B., Kashif, M., Veeradasan, P., Balakrishnan, S.R., Foo, K.L., Poopalan, P., 2015. PLOS One 10, 1–20.
Häkkinen, H., 2012. Nat. Chem. 4, 443–455.
Hosseini, Z.S., Mortezaali, A., Iraji, A., Fardindoost, S., 2015. J. Alloy. Comp. 628, 222–229.
Huang, H., Bai, W., Dong, C., Guo, R., Liu, Z., 2015. Biosens. Bioelectron. 68, 442–446.
Iyer, M.A., Oza, G., Velumani, S., Maldonado, A., Romero, J., Muñoz, M.D.L., Sridharan, M., Asomoza, R., Yi, J., 2014. Sens. Actuators B Chem. 202, 1338–1348.
Janotti, A., Van de Walle, C.G., 2009. Reports Prog. Phys. 72, 126501.
Jiang, R., Li, B., Fang, C., Wang, J., 2014. Adv. Mater. 26, 5274–5309.
Kashif, M., Ali, M.E., Ali, S.M.U., Hashim, U., Hamid, S.B.A., 2013. Nanoscale Res. Lett. 8, 1–9.
Kashif, M., Usman Ali, S.M., Ali, M.E., Abdulgafour, H.I., Hashim, U., Willander, M., Hassan, Z., 2012. Phys. Status Solidi 209, 143–147.
Khoa, N.T., Kim, S.W., Yoo, D.-H., Cho, S., Kim, E.J., Hahn, S.H., 2015. ACS Appl. Mater. Interfaces 7, 3524–3531.
Kochuveedu, S.T., Oh, J.H., Do, Y.R., Kim, D.H., 2012. Chem. Eur. J. 18, 7467–7472.
Köck, A., Chitu, L., Defregger, S., Kraker, E., Maier, G., Steinhauer, S., Wimmer-Teubenbacher, R., 2014. BHM 159, 385–389.
Kumar, R., Rana, D., Umar, A., Sharma, P., Chauhan, S., Chauhan, M.S., 2015. Talanta 137, 204–213.
Lakshmipriya, T., Fujimaki, M., Gopinath, S.C.B., Awazu, K., 2013. Langmuir 29, 15107–15115.
Lee, J., Shim, H.S., Lee, M., Song, J.K., Lee, D., 2011. J. Phys. Chem. Lett. 2, 2840–2845.
Li, J., Zhang, Y., To, S., You, L., Sun, Y., 2011. ACS Nano 5, 6661–6668.
Liu, Y., Zhong, M., Shan, G., Li, Y., Huang, B., Yang, G., 2008. J. Phys. Chem. B 112, 6484–6489.
McAlpine, M.C., Ahmad, H., Wang, D., Heath, J.R., 2007. Nat. Mater. 6, 379–384.
Mello, M.L.S., Vidal, B.C., 2012. PLOS One 7, 1–12.
Nomura, K., Gopinath, S.C.B., Lakshmipriya, T., Fukuda, N., Wang, X., Fujimaki, M., 2013. Nat. Commun. 4, 2855.
Ohno, R., Ohnuki, H., Wang, H., Yokoyama, T., Endo, H., Tsuya, D., Izumi, M., 2012. Biosens. Bioelectron. 40, 422–426.
Opdahl, A., Petrovykh, D.Y., Kimura-Suda, H., Tarlov, M.J., Whitman, L.J., 2007. Proc. Natl. Acad. Sci. U.S.A. 104, 9–14.
Perumal, V., Hashim, U., 2013. J. Appl. Biomed. 12, 1–15.
Perumal, V., Hashim, U., Gopinath, S.C.B., Haarindraprasad, R., Foo, K.L., Balakrishnan, S.R., Poopalan, P., 2015. Sci. Rep. 5, 12231.
Petrovykh, D.Y., Kimura-Suda, H., Whitman, L.J., Tarlov, M.J., 2003. J. Am. Chem. Soc. 125, 5219–5226.
Polsongkram, D., Chamninok, P., Pukird, S., Chow, L., Lupan, O., Chai, G., Khallaf, H., Park, S., Schulte, a, 2008. Phys. B Condens. Matter 403, 3713–3717.
Ramulu, T.S., Venu, R., Sinha, B., Lim, B., Jeon, S.J., Yoon, S.S., Kim, C.G., 2013. Biosens. Bioelectron. 40, 258–264.
Ryu, S.-W., Kim, C.-H., Han, J.-W., Kim, C.-J., Jung, C., Park, H.G., Choi, Y.-K., 2010. Biosens. Bioelectron. 25, 2182–2185.
Saif, A.A., Poopalan, P., 2011a. Solid. State. Electron. 62, 25–30.
Saif, A.A., Poopalan, P., 2011b. Phys. B Condens. Matter 406, 1283–1288.
Saif, A.A., Poopalan, P., 2011c. J. Alloy. Comp. 509, 7210–7215.
Shan, G., Zhong, M., Wang, S., Li, Y., Liu, Y., 2008. J. Colloid Interface Sci. 326, 392–395.
Simpson, R.E., Fons, P., Kolobov, a V., Fukaya, T., Krbal, M., Yagi, T., Tominaga, J., 2011. Nat. Nanotechnol. 6, 501–505.
Solanki, P.R., Kaushik, A., Agrawal, V.V., Malhotra, B.D., 2011. NPG Asia Mater. 3, 17–24.
Suh, D.I., Byeon, C.C., Lee, C.L., 2010. Appl. Surf. Sci. 257, 1454–1456.
Tak, M., Gupta, V., Tomar, M., 2014. Biosens. Bioelectron. 59, 200–207.
Wang, G., Huang, B., Li, Z., Lou, Z., Wang, Z., Dai, Y., Whangbo, M.-H., 2015. Sci. Rep. 5, 8544.
Wang, H.T., Kang, B.S., Ren, F., Tien, L.C., Sadik, P.W., Norton, D.P., Pearton, S.J., Lin, J., 2005. Appl. Phys. A Mater. Sci. Process. 81, 1117–1119.
Wang, J., Li, S., Zhang, Y., 2010a. Electrochim. Acta 55, 4436–4440.
Wang, L., Sun, Y., Wang, J., Wang, J., Yu, A., Zhang, H., Song, D., 2010b. J. Colloid Interface Sci. 351, 392–397.
Wang, X., Wang, W., Liu, Y.-L., 2012. Sens. Actuators B Chem. 168, 39–45.
Wu, J.-J., Tseng, C.-H., 2006. Appl. Catal. B Environ. 66, 51–57.
Zhang, J., Que, W., 2010. Sol. Energy Mater. Sol. Cells 94, 2181–2186.
Zhang, W., Yang, T., Huang, D., Jiao, K., Li, G., 2008a. J. Memb. Sci. 325, 245–251.
Zhang, W., Yang, T., Huang, D.M., Jiao, K., 2008b. Chin. Chem. Lett. 19, 589–591.
Zhang, X.D., Guo, M.L., Shen, Y.Y., Liu, C.L., Xue, Y.H., Zhu, F., Zhang, L.H., 2012. Comput. Mater. Sci. 54, 75–80.